




OPEN

Use of silica-based homogeneously distributed gold nickel nanohybrid as a stable nanocatalyst for the hydrogen production from the dimethylamine borane

Oznur Alptekin¹, Betül Sen², Aysun Savk², Umran Ercetin¹✉, Sibel Demiroglu Mustafov², Mehmet Ferdi Fellah³ & Fatih Sen² ✉

In this study, the effects of silica-based gold-nickel (AuNi@SiO₂) nanohybrid to the production of hydrogen from dimethylamine borane (DMAB) were investigated. AuNi@SiO₂ nanohybrid constructs were prepared as nanocatalysts for the dimethylamine borane dehydrogenation. The prepared nanohybrid structures were exhibited high catalytic activity and a stable form. The resulting nanohybrid, AuNi@SiO₂ as a nanocatalyst, was tested in the hydrogen evolution from DMAB at room temperature. The synthesized nanohybrids were characterized using some analytical techniques. According to the results of the characterization, it was observed that the catalyst was in nanoscale and the gold-nickel alloys showed a homogenous distribution on the SiO₂ surface. After characterization, the turn over frequency (TOF) of nanohybrid prepared for the production of hydrogen from dimethylamine was calculated (546.9 h⁻¹). Also, the prepared nanohybrid can be used non-observed a significant decrease in activity even after the fifth use, in the same reaction. In addition, the activation energy (E_a) of the reaction of DMAB catalyzed AuNi@SiO₂ nanohybrid was found to be 16.653 ± 1 kJmol⁻¹ that facilitated the catalytic reaction. Furthermore, DFT-B3LYP calculations were used on the AuNi@SiO₂ cluster to investigate catalyst activity. Computational results based on DFT obtained in the theoretical part of the study support the experimental data.

Today, the decreasing fossil fuels, the enhancing environmental problems and the dependence on energy caused a much tendency towards alternative energy sources. Therefore, hydrogen as a clean, highly efficient and non-toxic energy storage chemical has influenced scientists^{1–3}. However, problems with the storage of hydrogen continue. Storage of hydrogen in gas and liquid phase is very difficult and costly. Therefore, the orientation towards hydrogen removal from some hydrogen storage materials has begun. Recently, especially Sodium Borohydride (NaBH₄) (SBH) and Ammonia borane (AB) derivatives have been used economically and high efficiency^{4–6}. Sodium Borohydride (SBH) (NaBH₄) has a high hydrogen content of 10.8% and its usage is easy. Ammonia borane derivatives (AB) are a great source of energy because they have a 19.6% hydrogen content and have high stability^{7,8}. In the presence of a proper catalyst, ammonia borane derivatives have a very high capacity to produce hydrogen. Numerous catalysts were utilized to produce hydrogen from ammonia boranes (ABs). The use of dimethylamine-borane, which is an AB derivative in the dehydrogenation of nanohybrid showing high catalytic activity, is highly advantageous in terms of yield^{9–25}. The identification of products released after the hydrogen production reaction of dimethylamine borane (Eq. 1) compared to the other AB product is relatively simple. In hydrogen production from DMAB, as the derivatives of other ABs, catalysts are usually required for f-metal complexes. For this purpose, f-metal nanohybrids have been widely used and have been studied to be highly efficient^{15,26–33}. For this purpose, high efficiency, stable, silica (SiO₂) based AuNi nanohybrid (AuNi@SiO₂) was

¹Department of Mechanical Engineering, Faculty of Engineering, Dumlupınar University, Evliya Çelebi Campus, 43100, Kütahya, Turkey. ²Sen Research Group, Department of Biochemistry, Faculty of Art and Science, Dumlupınar University, Evliya Çelebi Campus, 43100, Kütahya, Turkey. ³Department of Chemical Engineering, Bursa Technical University, Mimar Sinan Campus, 16310, Bursa, Turkey. ✉e-mail: umran.ercetin@dpu.edu.tr; fatih.sen@dpu.edu.tr

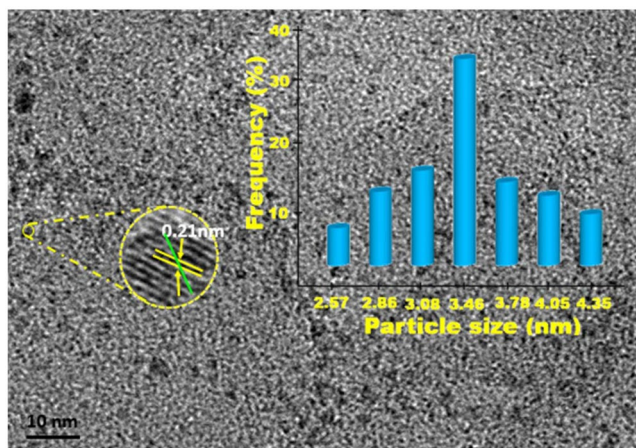
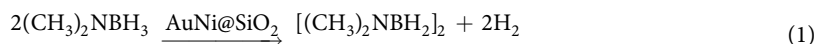


Figure 1. AuNi@SiO₂ nanohybrid TEM, HR-TEM, and particle size histogram.

synthesized for use in dehydrogenation of dimethylamine borane. For the dehydrogenation of the dimethylamine borane, the ultrasonic reduction method was employed to synthesize homogeneously dispersed AuNi nanohybrid with silica support. Then, the characterization of the synthesized nanohybrid was carried out employing some analytical methods like XPS, TEM, XRD, and HR-TEM analytical techniques. The prepared AuNi@SiO₂ nanohybrid, using the ultrasonic reduction, tested at different amount of catalyst concentration for hydrogen evolution in the dehydrogenation of DMAB reaction. In view of the values found, the activation values, catalytic activity, turnover frequency and reusability of the nanohybrid used were investigated. It is noteworthy that the AuNi@SiO₂ nanohybrid synthesized exhibited, according to the result of these investigations, a relatively high cycle frequency compared to other nanocatalysts in the literature.



Experimental

In our study, it was aimed to prepare SiO₂ based AuNi nanohybrid using the ultrasonic reduction method. For this purpose, 0.25 mmol AuCl₃ and NiCl₂ were mixed in the ultrasonic sonicator and 2.5 mmol SiO₂ was added as support. The resulting mixture was mixed using a magnetic stirrer to homogenize. Then, superhydride was added to the resulting solution, and then color change in solution was observed. This shows us that the particles (Au³⁺ and Ni²⁺) are reduced and nanohybrid formed. The Au³⁺ and Ni²⁺ cations have high stability by reducing to Au (0) and Ni (0). Dimethylamine borane was added to the nanocatalyst synthesized at room temperature (25 °C) and hydrogen output was examined during the reaction. XPS, TEM, XRD, and HR-TEM analytical techniques were used to investigate the characterization, structural morphology, particle size and content nanoparticles. In addition, stability, catalytic activity, activation parameters, efficiency and cycle frequency of nanohybrid, which are intended to make the reaction more active during dehydrogenation entered by DMAB, were evaluated.

Computational method. The theoretical calculations which are employed for the structures in this study have been based on Density Functional Theory (DFT)³⁴. The software of Gaussian 09³⁵ has been used with the B3LYP-Hybrid method^{36,37}. The basis set of LanL2DZ has been utilized in calculations for Au and Ni atoms. The basis set which is utilized for C, O and H atoms (the rest atoms in the structures) in a cluster is 6-31G (d, p) basis set.

The SiO₂ cluster used for calculations has Si atoms and Oxygen atoms. The cluster was modeled as (002) surface. The SiO₂ cluster structure was shown in the Supporting Information in Fig. S1. Dangling bonds of the O atoms have been saturated with H atoms to obtain a neutral cluster. To obtain the AuNi@SiO₂ cluster representing the AuNi@SiO₂ catalyst, Au and Ni atom were used. In this study, all atoms of the structures were relaxed in the course of all DFT calculations. The details of the theoretical strategy utilized in the theoretical part of this study have been stated in Supporting Information (Tables S1 and S2).

Results and Discussion

As a result of DMAB dehydrogenation reaction catalyzed with AuNi@SiO₂ nanohybrid synthesized by ultrasonic method, structural analyzes of the nanocatalyst and its catalytic activity in hydrogen production were evaluated. XPS, TEM, XRD, B-NMR, SEM-EDX and HR-TEM techniques were used for the characterization of AuNi@SiO₂ nanohybrid. Firstly, TEM and HRTEM methods were utilized to determine the morphology and particle size of nanohybrids. Figure 1 shows the synthesized nanohybrids as homogeneous and monodisperse on the SiO₂ support material according to these methods. It was observed that the particles were not randomly clustered and accumulated and were stable in the spherical structure. According to these results, the particle size of AuNi@SiO₂ nanohybrid was calculated to be 3.46 ± 0.89 nm. As shown in Fig. 1, HR-TEM was employed to show the nanohybrid AuNi@SiO₂ synthesized atomic lattice fringes. When the results are compared with the literature, it has been confirmed that they are compatible with the literature. 11B-NMR study of the reaction showed that the

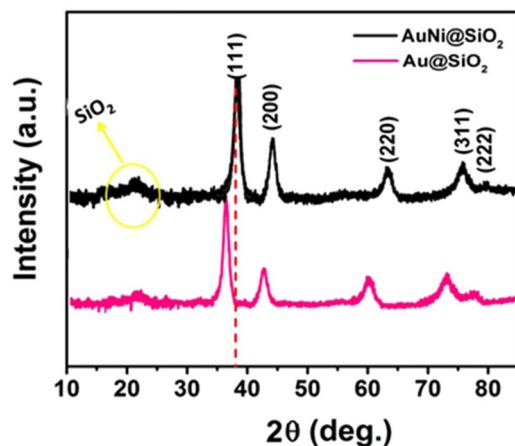


Figure 2. XRD patterns of Au@SiO₂ and AuNi@SiO₂ nanohybrid.

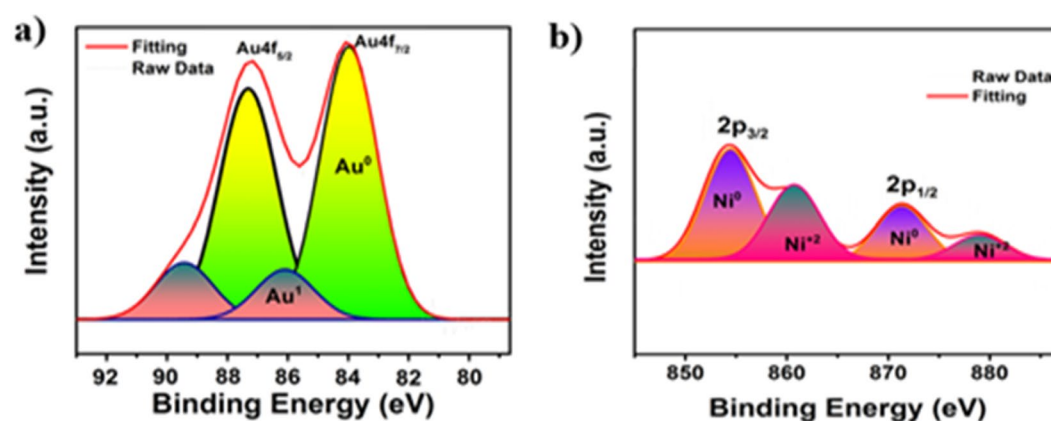


Figure 3. (a) XPS spectra of Au 4f and (b) Ni 2p AuNi@SiO₂ nanohybrids.

dimethylamine borane (DMAB) and the catalytic dehydrogenation of dimethylamine borane in the presence of AuNi@SiO₂ at room temperature (Supporting Information, Fig. S4).

As a result of the introduction of Ni atoms into the Au lattice structure, the distortion of the lattice structure of gold occurs. Accordingly, the lattice parameters are expected to decrease after an alloy of AuNi formation. In order to explain this situation, the XRD curve of the nanohybrid having the highest active surface area was taken and compared with the XRD result of pure Au. The comparison of XRD curves is given in Fig. 2. Here, we see curves (111), (220) and (311) in the surface-centered cubic structure of gold. The most intense breaking peak for Au is (111). This value indicates that (111) is the most preferred growth direction of the Au core and then, is directly approved by HR-TEM. In Fig. 2, the $2\theta = 38.3^\circ$ scatter curve for all nanohybrid is caused by the catalyst support material. In short, Fig. 2 demonstrates the formation of AuNi alloy nanohybrid materials. In Figs. S5 and S6, the XRD pattern and SEM image of after-use AuNi@SiO₂ nanohybrids for H₂ production is given in Supporting Information, respectively.

For the characterization oxidation state of Au and Ni in the prepared catalyst sample, XPS analysis was performed. The determination of gold and nickel on the surface of the prepared nanohybrid structure is shown by the XPS results in Fig. 3; Ni-2p_{3/2} and Ni-2p_{1/2} peaks at 87.3 eV and 84.5 eV found in Au-4f_{5/2} and Au-4f_{7/2} peaks at 850.2 eV and 870.2 eV, respectively. Referring to Fig. 3, it can be said that most of the Au and Ni nanohybrid is zero-valued, and a small amount of Au⁺³ and Ni⁺² valence. The lower energy shift of the gold and nickel binding XPS energies shows the character of the alloy. As a result of homogenous distribution of AuNi on SiO₂ nanohybrid during synthesis, more zero oxidation peaks were observed. According to these data, we can explain that gold and nickel have a very good bonding structure and have a monodispers alloy nanohybrids. Furthermore, the survey spectra of AuNi@SiO₂ nanohybrids were given in Supporting Information (Fig. S7). The results of XPS analysis for chemical composition and elemental percentages of AuNi@SiO₂ nanohybrids were given in Supporting information (Tables S3 and S4). EDX analysis from four different areas and the element mapping results of the catalyst were given in Fig. S8 and Table S5 to better understand whether the synthesized catalyst forms alloy or core-shell.

In our study, the efficacy of synthesized AuNi@SiO₂ nanohybrid in the reactions of DMAB was tested. Figure 4A shows the amount of hydrogen produced by dehydrogenation of DMAB with different amounts of AuNi@SiO₂ nanohybrid as 2.25, 4.50, 6.75 and 9.00 mM at $25.0 \pm 0.1^\circ\text{C}$. Figure 4A shows the hydrogen

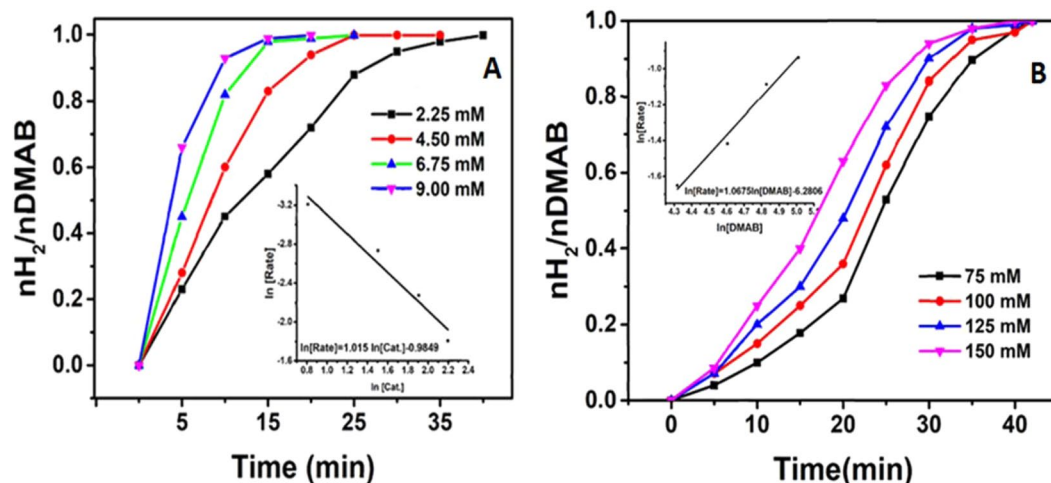


Figure 4. (A) DMAB graphical drawing of molar H_2 /mol against time in the existence of $AuNi@SiO_2$ at varied catalyst concentrations at 25.0 ± 0.1 °C, (B) DMAB graphical drawing of molar H_2 /mol against time at different substrate concentrations catalyzed by $AuNi@SiO_2$ for dehydrogenation of dimethylamine borane.

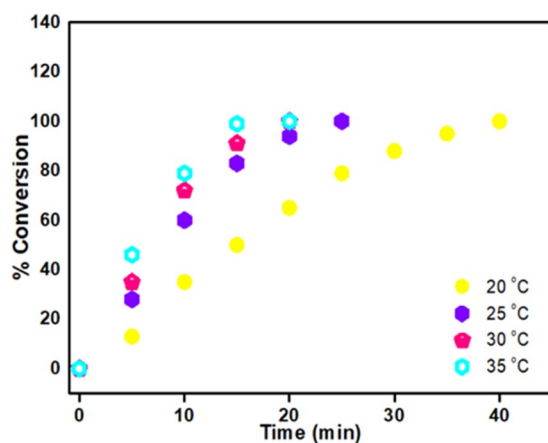


Figure 5. Time-dependent % conversion graph at different temperatures for dehydrogenation of dimethylamineborane.

production rate and the linear part of each slope line for the catalytic reaction DMAB catalyzed $AuNi@SiO_2$ nano hybrid. According to these calculations, the rate of hydrogen release is seen to grow as the catalyst amount increases. Also, in Fig. 4A, the slope of the plot is given as 1.015. According to this result, it is clear that the rate of reaction of hydrogen production depends on the amount of catalyst in the first order. Experiments to investigate the effect of dimethylamine borane on the catalytic reaction at room temperature were conducted using different amounts. The results obtained for this purpose are shown in Fig. 4B. According to these results, the amount of hydrogen produced by $AuNi@SiO_2$ nano hybrid in different amounts (75, 100, 150 and 200 mM) was investigated. Also, in Fig. 4B, the slope of the plot is found as 1.0675. According to this result, it is clear that the rate of reaction of hydrogen production is dependent on the amount of DMAB in the first order.

The dimethylamine borane dehydrogenation reaction with $AuNi@SiO_2$ nano hybrid was performed at different temperatures (20, 25, 30, 35 °C). As displayed in Fig. 5a, at four different temperatures, the rate constants for dehydrogenation of dimethylamine borane were determined. Arrhenius and Eyring graphs obtained with these calculations are given in Fig. 6a,b. As a result of the calculations based on Arrhenius and Eyring graphics; $E_a = 26.013$ kJmol⁻¹, $\Delta H = 23.51$ kJmol⁻¹, $\Delta S = -122.83$ kJmol⁻¹. It has been observed that $AuNi@SiO_2$ nano hybrid used in dehydrogenation of dimethylaminborane exhibits very good catalytic performance compared to the literature studies.

NMR data obtained as a result of this study shows that $(CH_3)_2NHBH_3$ ($\delta = 712,7$ ppm) provides complete conversion to $[(CH_3)_2NBH_2]_2$ ($\delta \sim 5$ ppm). Thus, even at room temperature (at 25 °C), it can be seen that the amount of dimethylamine borane dehydrogenation yields 1.0 equivalent H_2 .

The TOF value of $AuNi@SiO_2$ nano hybrid, which has a high level of stability for dehydrogenation of dimethylamine borane and its activation parameters is 546.9 h⁻¹ as listed in Table 1. This value is one of the best values

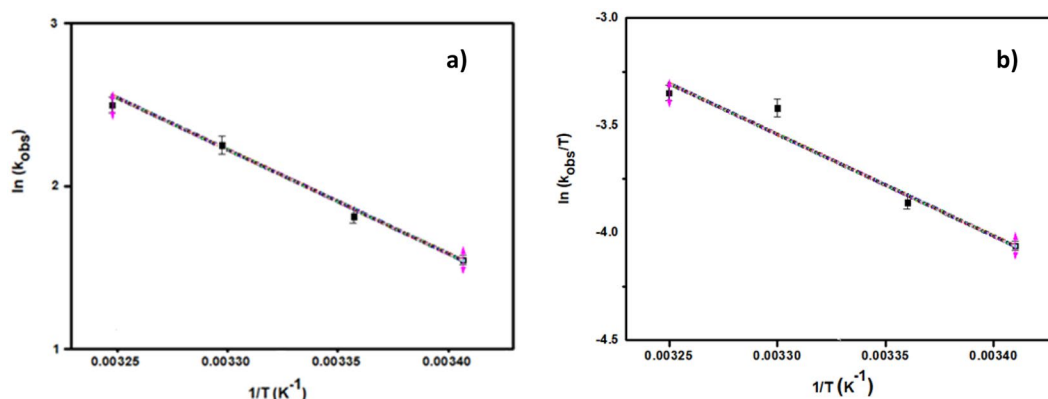


Figure 6. (a) Arrhenius parcel at different temperatures, (b) Eyring parcel at different temperatures.

according to TOF values of catalysts in literature. Namely, the monodisperse AuNi@SiO₂ nanohybrid prepared for the hydrogen production from the dimethylamine borane has been rapidly converted at room temperature. This indicates that the efficiency of the nanocatalyst obtained is high.

The very good activation parameters of AuNi@SiO₂ nanohybrid can be described by Au and Ni synergistic effect on the homogeneous distribution of nanohybrid on a support material, the catalytic activity of Au (0) and Ni (0) percentages, small particle size and the large surface area of nanohybrid.

The reusability of synthesized nanohybrid is one of the important factors for both cost and easy application. For this purpose, re-usability of the produced AuNi@SiO₂ nanohybrid was evaluated. As shown in Fig. 7, the AuNi alloy nanohybrid on the SiO₂ support material maintained its catalytic activity with approximately 84% of its initial performance even at the end of the fifth experiment in the dehydrogenation reaction with DMAB. However, in the ongoing trials, the AuNi@SiO₂ nanocatalysts decreased their catalytic activity due to increased aggregation and reduced surface area. However, its reusability is tremendously good. AuNi@SiO₂ nanohybrid, which has a high conversion frequency, showed superior catalytic performance as a high-yield catalyst for the dehydrogenation of dimethylamine borane. The stable and efficient structure of Au and Ni nanohybrid is due to the SiO₂ support material employed in the preparation of nanohybrid. The increase in surface area of the AuNi alloy due to the silica-based support agent has led to increased efficiency. In summary, according to studies and calculations, the surface area of the expanded AuNi@SiO₂ nanohybrid with silica provided a very high TOF value (546.9 h⁻¹). At the same time, the calculated activation energy value $E_a = 26.013 \text{ kJmol}^{-1}$ is among the lowest activation energies in the literature for DMAB dehydrogenation reaction.

In order to clarify the activity of AuNi@SiO₂ catalyst, the theoretical calculations have been utilized. For this purpose, initially, SiO₂ cluster was optimized by EG calculation. The optimized SiO₂ cluster structure is shown in the Supporting Information in Fig. S2. Then AuNi@SiO₂ cluster was optimized geometrically by utilizing EG calculations. For this AuNi@SiO₂ cluster optimization, neutral charge and doublet SM were used. The minimum SPE energy of the cluster corresponds to the sextet SM. Similarly, the doublet SM was obtained for the structure containing the AuNi@SiO₂ cluster with a DMAB molecule. Figure 8 indicates EGs for AuNi@SiO₂ cluster. The charge and SM for the adsorbing molecule (DMAB molecule) have been determined as neutral and singlet, respectively. The DMAB molecule's optimized geometry has been represented in Fig. 8.

After obtaining the optimized geometries of cluster and adsorbing molecule (DMAB), adsorption of the DMAB molecule has been examined on AuNi@SiO₂ cluster by optimization (EG) calculations. Two probabilities according to the position of the DMAB molecule on the catalyst surface for the DMAB adsorption on AuNi@SiO₂ cluster have been mentioned for EG calculations. These positions have been represented in Fig. S3 in Supporting Information. For these structures, total energy values (containing zero point energy correction) with DMAB adsorption on the AuNi@SiO₂ cluster were determined to be $-15783.831058 \text{ a.u.}$ and $-15783.903295 \text{ a.u.}$ respectively, which suggests that DMAB adsorption is most suitable for configuration 2. For this configuration, optimized geometry for adsorbed DMAB molecule is shown in Fig. 9 on AuNi@SiO₂ cluster. It can be shown that the DMAB molecule was adsorbed on Ni atom of the AuNi@SiO₂ cluster.

The adsorption energy (ΔE), enthalpy (ΔH), and Gibbs free energy (ΔG) values for DMAB adsorption have been computed by using equation 8 in Supporting Information. Furthermore, chemical potential, ΔE , and ΔG , chemical hardness, electronegativity, electrophilicity, and HLG values were computed for both α and β molecular orbitals (spin up and spin down, respectively). These values which have been tabulated in Table 2 were calculated by using the HOMO/LUMO values of the optimized AuNi@SiO₂ cluster-DMAB system^{38,39}. For the optimized AuNi@SiO₂ cluster-DMAB structure, the values were calculated employing equations 4–7 in Supporting Information where $I \cong -\epsilon_{HOMO}$ and $A \cong -\epsilon_{LUMO}$. In addition, the chemical potential value has been determined by utilizing equation 5 in Supporting Information where $I \cong -\epsilon_{HOMO}$ of free DMAB and $A \cong -\epsilon_{LUMO}$ of the AuNi@SiO₂ cluster^{21,38–41}.

Before the DMAB molecule adsorption, the values of chemical potential for α and β molecular orbitals (MOs) have been computed as -151.0 and -156.3 respectively by using equation 5 in Supporting Information where $I \cong -\epsilon_{HOMO}$ of free DMAB molecule and $A \cong -\epsilon_{LUMO}$ of the AuNi@SiO₂ cluster^{21,38–41}. These values designate

Entry	(Pre) Catalysts	Conv. %	TOF (Turnover Frequency)	Ref.
1	AuNi@SiO ₂	100	546.9	This Study
2	Carbon Stabilized Palladium particles	95	2.8	49
3	Grafen oxide-based Ruthenium nanoparticles	100	410.01	50
4	Rhodium (III) chloride	90	7.9	49
5	Iridium (III) chloride	25	0.3	49
6	Ruthenium (III) chloride	77	2.7	49
7	Vulcan Carbon-based Pt nanoparticles	100	23.14	26
8	BA-based Platinum nanomaterials	100	24.8	18
9	TBA-based Platinum nanoparticles	100	31.24	18
10	Polymer supported Ruthenium-Nickel	100	458.57	19
11	Amylamine stabilized Platinum Nanoparticles	100	15.00	20
12	Activated Carbon Stabilized Pt Nanoparticles	100	34.14	21
13	PVP stabilized Palladium-Cobalt nanoparticles	100	330.00	22
14	Grafen oxide-based RuPtNi nanomaterials	100	727.00	23
15	Carbon nanotube-based Ruthenium-cobalt nanoparticles	100	775.28	24
16	PEDOT supported Palladium Nickel Nanoparticles	100	451.28	29
17	Polymer-graphene based Platinum Nanomaterials	100	42.94	25
18	Graphene oxide stabilized Palladium-Nickel Nanomaterials	100	271.90	32
19	Graphene oxide-based Palladium Nanoparticles	100	38.02	11
20	Carbon black hybrid supported platinum nanomaterials	100	70.28	26

Table 1. TOF values of catalysts for dehydrogenation of dimethylamine borane.

that AuNi@SiO₂ cluster has a high value of chemical potential for the DMAB molecule interaction. AuNi@SiO₂ cluster' activity based on electrophilicity, electronegativity, chemical hardness and potential values has been obtained. The chemical potential has been related to the adsorption energy. Then, if a cluster has a low chemical potential, the adsorption energy of DMAB on the cluster is also comparatively low^{42,43}. Afterward, the DMAB molecule adsorption on AuNi@SiO₂ cluster, the chemical hardness, the HOMO-LUMO gap (HLG) and the chemical potential values have reduced as the electronegativity and the electrophilicity values have risen. Additionally, ΔG for DMAB molecule adsorption on AuNi@SiO₂ cluster has been determined to be -42.3 kcal/mol, which designates DMAB molecule adsorption happens instantaneously on the AuNi@SiO₂ cluster. The relative energy adsorption value for the adsorbing molecule adsorption has been computed as -56.6 kcal/mol on the AuNi@SiO₂ cluster meaning DMAB molecule has been strongly adsorbed on it.

The HLG was widely used as a measure of kinetic stability, and it was commonly recognized that if the gap between HOMO and LUMO is narrow, the kinetic stability is weak and the chemical reactivity is good. In the

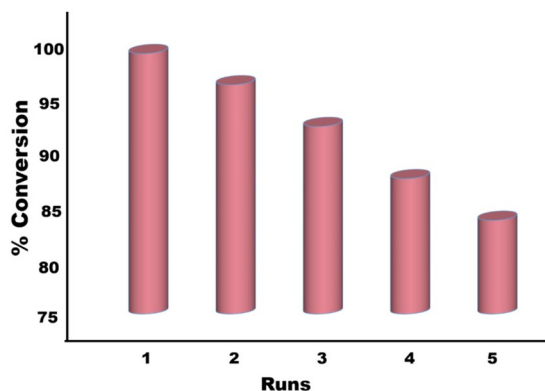


Figure 7. Plots of % conversion versus time for AuNi@SiO₂ catalyzed dehydrogenation of DMAB at room temperature for 1st and 5th catalytic runs.

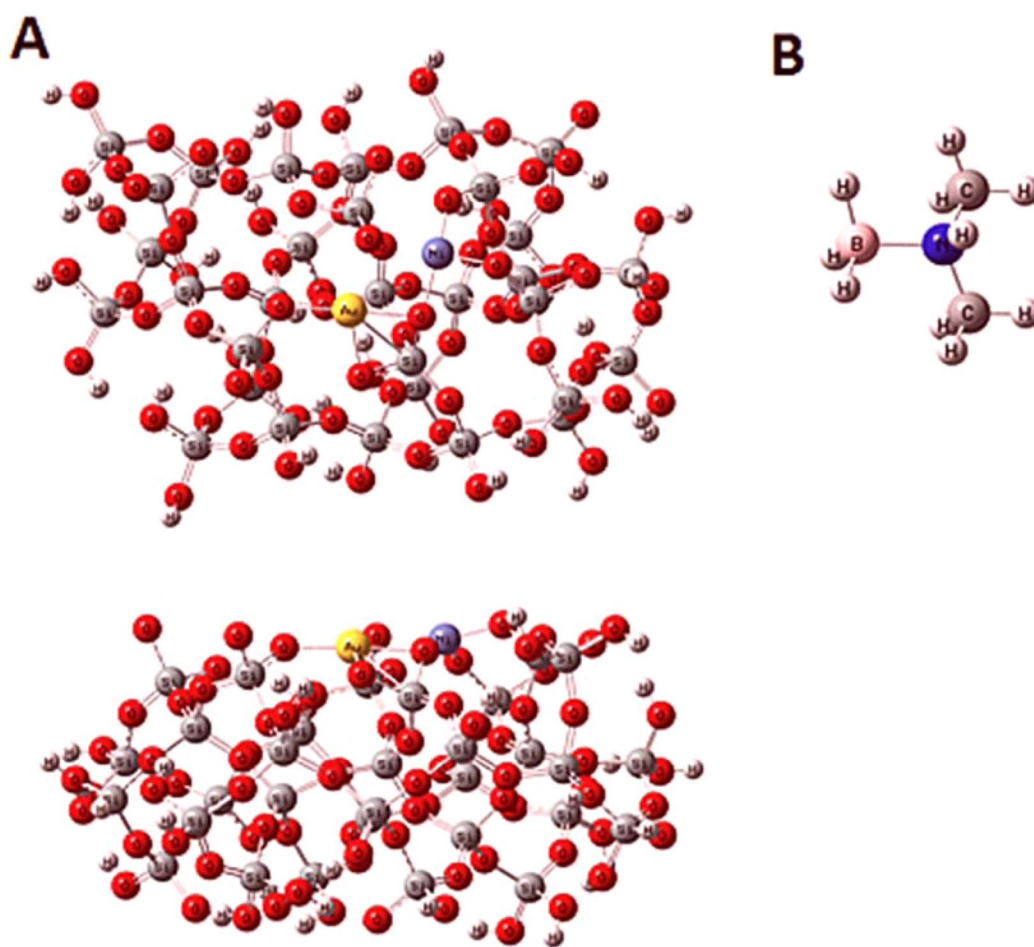


Figure 8. Optimized structures (A) AuNi@SiO₂ cluster (top view and side view) and (B) molecule DMAB.

meantime, it defines energetically opportune for the HOMO losing electrons or gaining electrons of the LUMO. According to the Table 2, it has been obviously stated that the α -HLG and β -HLG values of 56.9 kcal/mol and 46.3 kcal/mol respectively for the AuNi@SiO₂ cluster is meaningfully smaller than the HOMO-LUMO gap value of 100.4 kcal/mol for the SiO₂ cluster. After this, it might be clearly concluded that the SiO₂ cluster's chemical reactivity was knowingly improved by Au and Ni atoms addition on the SiO₂ cluster. In other words, the AuNi@SiO₂ cluster's chemical reactivity is higher than the chemical reactivity of the SiO₂ cluster. The HOMO and LUMO distributions of α and β electrons for the AuNi@SiO₂ cluster are indicated in Fig. 10. It was obviously stated that LUMOs of α and β electrons were located on Ni atom for the AuNi@SiO₂ cluster. So, this clarifies that the DMAB molecule has been adsorbed on Ni atom of the AuNi@SiO₂ cluster. The chemical potential values for the AuNi@

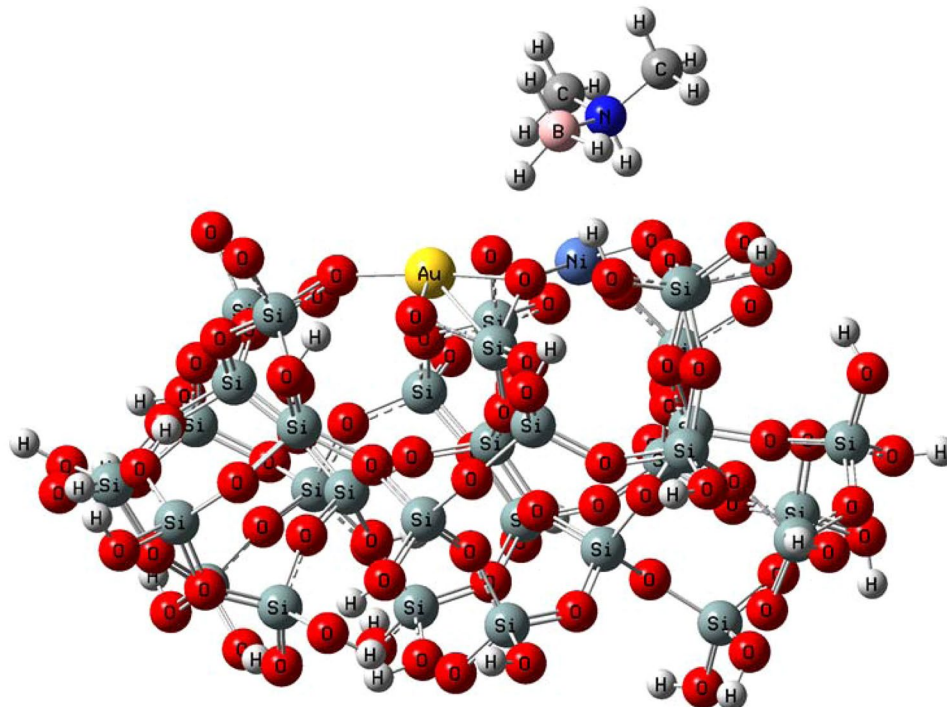


Figure 9. Optimized structure of DMAB molecule adsorbed on AuNi@SiO₂ cluster.

Properties	AuNi@SiO ₂ Cluster		AuNi@SiO ₂ Cluster with adsorbed DMAB	
	α MO (Spin Up)	β MO (Spin down)	α MO (Spin Up)	β MO (Spin Down)
HOMO	-193.0	-193.0	-185.7	-185.7
LUMO	-136.1	-146.7	-149.0	-139.9
Chemical Hardness	28.4	23.2	18.3	22.9
Chemical Potential	-164.6	-169.9	-167.4	-162.8
Electronegativity	164.6	169.9	167.4	162.8
Electrophilicity	476.1	623.2	763.8	578.1
HLG	56.9	46.3	36.7	45.9
ΔE	—	—	-56.0	
ΔH	—	—	-56.6	
ΔG	—	—	-42.3	

Table 2. Comparison of hydrogen adsorption energy values (Energy values are in units of kcal/mol). The HOMO and LUMO values of optimized SiO₂ cluster were calculated to be 162.7 and 62.4 kcal/mol, respectively.

SiO₂ cluster have been decreased after the DMAB molecule adsorption meaning the active site of the AuNi@SiO₂ cluster has still the activity for the other DMAB molecules.

Additionally, Fig. 11a,b show ED distribution map for AuNi@SiO₂ cluster. Such representations have shown that the densities of electrons are mostly found on the atoms of Au and Ni. ELF distribution map^{36,44–46} has been shown in Fig. 11c,d for AuNi@SiO₂ cluster. The ELF distribution is a valued tool to obtain the place of electron pairs⁴⁶. The role of electronic localization provides understanding of the empirical principle of electron localization, in particular, pair electron localization. Depending on the electronic localization function graph, the atoms in which they exhibited larger values of the electronic localization function in AuNi@SiO₂ cluster are Au and Ni atoms. Moreover, the negative and positive distribution of electrostatic potential (ESP) regions (Fig. 12) on the surface of the van der Waals was shown between the colors red and blue^{47,48}. Analysis of the ESP distribution of AuNi@SiO₂ cluster data demonstrations that positive regions are located smoothly on Au and Ni atoms (mainly Ni atom). This is consistent with the distribution of charges for Au and Ni atoms (+0.417 and +0.738, respectively) gathered by Mulliken population analysis. It should be also mentioned that some blue regions (positive) of AuNi@SiO₂ cluster have been located around the surrounding hydrogen atoms. However, it is not appropriate to regard this since these hydrogen atoms have been utilized for saturating atoms for AuNi@SiO₂ cluster. In addition,

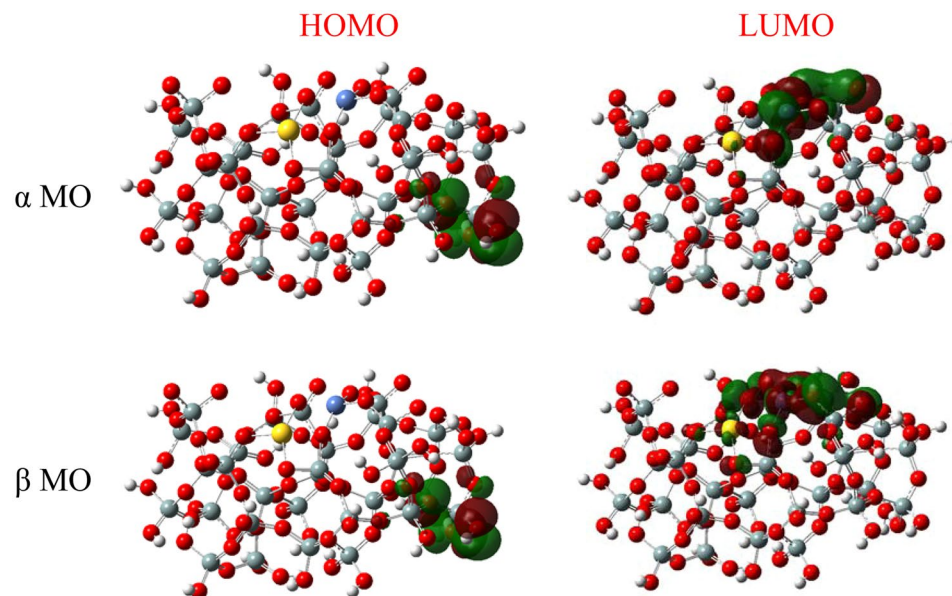


Figure 10. The HOMO/LUMO distributions of α and β MOs for the optimized AuNi@SiO₂ cluster.

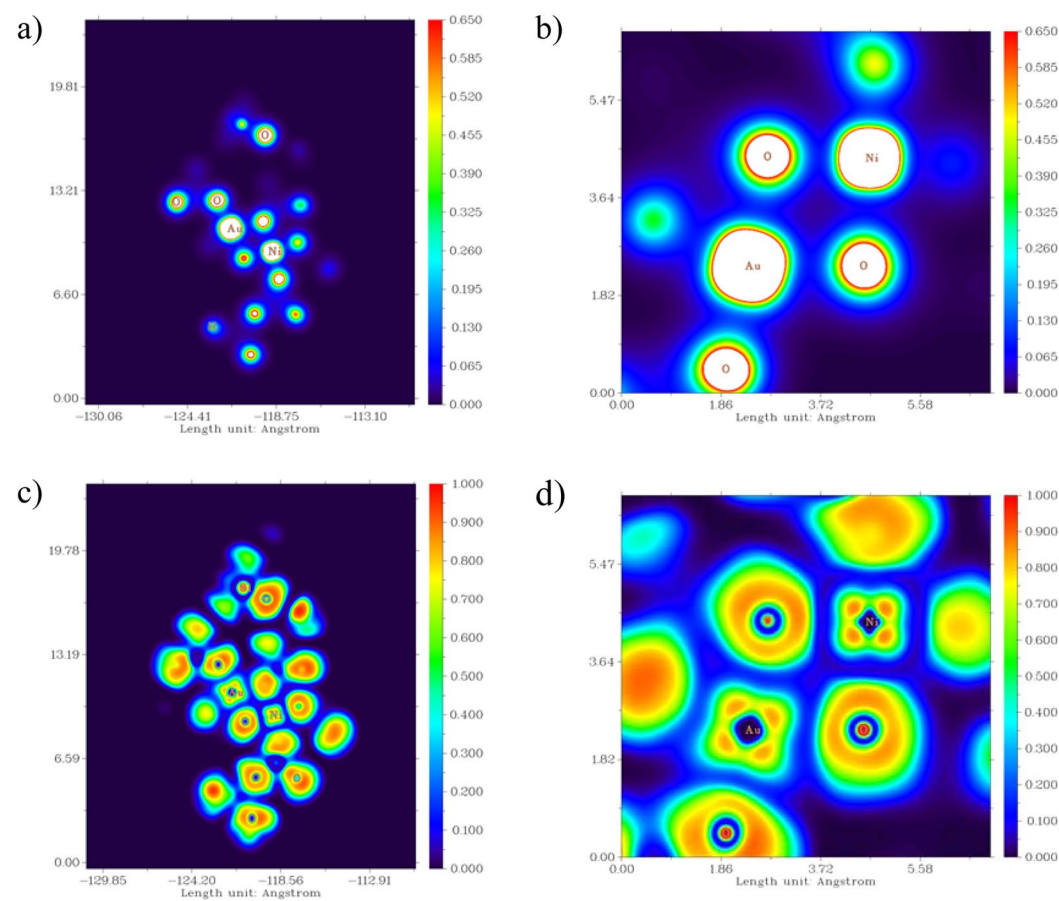


Figure 11. Distribution map of electron density (ED) for optimized AuNi@SiO₂ cluster; (a) at cluster level and (b) at Au and Ni atoms level of the cluster, distribution map of electronic localization function (ELF) for optimized AuNi@SiO₂ cluster; (c) at cluster level and (d) at Au and Ni atoms level of the cluster.

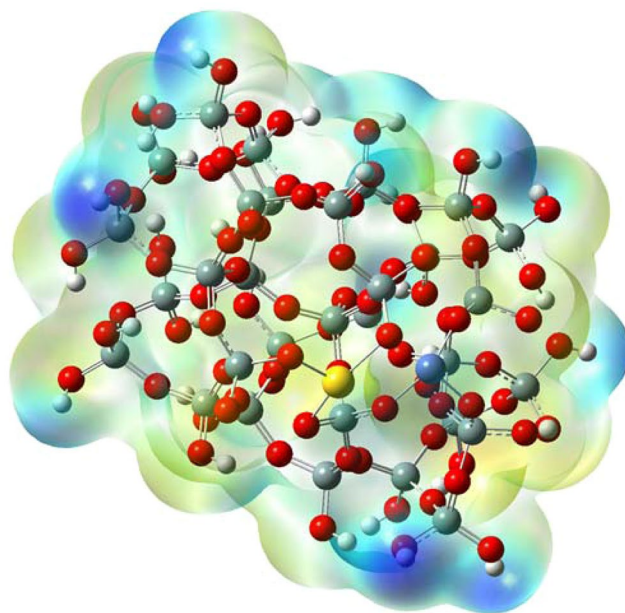


Figure 12. ESP distribution for optimized AuNi@SiO₂ cluster.

Metal Atom	α and β Molecular Orbitals (Spin Up/Spin Down)	The occupation numbers of 5d and 3d orbitals					Total occupation numbers of 5d and 3d orbitals
		dx _{xy}	dx _z	dy _z	dx ² -y ²	dz ²	
Au	α MO	0.760	0.949	0.985	0.867	0.958	9.040
	β MO	0.758	0.949	0.984	0.869	0.959	
Ni	α MO	0.927	0.995	0.997	0.710	0.985	8.267
	β MO	0.830	0.391	0.914	0.573	0.946	

Table 3. The computed occupation numbers of 5d and 3d orbitals for Au and Ni atoms respectively in optimized the AuNi@SiO₂ cluster.

the occupation numbers of 5d and 3d orbitals for Au and Ni atoms respectively in optimized AuNi@SiO₂ cluster have been calculated with respect to NPA analysis and have been listed in Table 3. These results are relatively in consistent with the XPS results that represent the oxidation states of gold and nickel present on SiO₂ catalysts.

Conclusions

The present study paves ways for controlled synthesis of AuNi@SiO₂ nanohybrid with ultrasonic reduction method and towards promising practical applications. It was characterized by XRD, XPS, TEM, and HR-TEM analysis to better understand synthesized nanohybrid while producing a novel AuNi@SiO₂ nanohybrid with an efficient, clean and environmentally friendly method. The prepared AuNi@SiO₂ nanohybrid was successfully applied in dehydrogenation of DMAB reactions. Thanks to Au and Ni, carbon-free and non-porous SiO₂ support, AuNi@SiO₂ nanohybrids formed stable and efficient nanostructures. Furthermore, the AuNi alloy on the support material was homogeneously distributed and very tightly bonded. As given previously in Table 1, AuNi@SiO₂ nanohybrid in the hydrogen production reaction of dimethylamine borane for the production of hydrogen has a high TOF value (546.9 h⁻¹), stability and catalytic activity. At the same time, in the dehydrogenation reaction of the obtained nanohybrid with dimethylamine borane, the fact that it continues its activity with approximately 84% of its first performance even in the fifth attempt that is an indicator of its very successful catalytic property. In addition, according to the data obtained from the hydrogen - DMAB graph, it was found that the rate of hydrogen production was the first-order dependent on AuNi@SiO₂ nanohybrids and DMAB amount. According to the results of the numerical analysis, the activation values were obtained as $E_a = 26.013 \text{ kJmol}^{-1}$, $\Delta H = 23.51 \text{ kJmol}^{-1}$, $\Delta S = -122.83 \text{ kJmol}^{-1}$. When these values are examined, it is noteworthy that the activation energy is very low. As a result, AuNi@SiO₂ nanohybrids can be considered as a promising catalyst with excellent catalytic performance, simple handling, very good reusability, and high stability for hydrogen production and storage at room temperature. Theoretical data depending on LUMO, HOMO chemical hardness, electronegativity, chemical potential, ΔE , ΔH , and ΔG values as well as ED, ELF and ESP distributions obtained in the theoretical part of the study supports the experimental data which is consequently high activity of the DMAB dehydrogenation catalyst AuNi@SiO₂.

Received: 12 December 2019; Accepted: 12 April 2020;

Published online: 29 April 2020

References

- Barreto, L., Makihira, A. & Riahi, K. The hydrogen economy in the 21st century: A sustainable development scenario. *Int. J. Hydrogen Energy* **28**, 267–284 (2003).
- Mohanty, S., Babu, P., Parida, K. & Naik, B. Surface-Plasmon-Resonance-Induced Photocatalysis by Core-Shell SiO₂@Ag NCs@Ag₃PO₄ toward Water-Splitting and Phenol Oxidation Reactions. *Inorg. Chem.* **58**, 9643–9654 (2019).
- Babu, P., Mohanty, S., Naik, B. & Parida, K. Synergistic Effects of Boron and Sulfur Co-doping into Graphitic Carbon Nitride Framework for Enhanced Photocatalytic Activity in Visible Light Driven Hydrogen Generation. *ACS Appl. Energy Mater.* **1**, 5936–5947 (2018).
- Lee, J. *et al.* A structured Co-B catalyst for hydrogen extraction from NaBH₄ solution. *Catal. Today* **120**, 305–310 (2007).
- Mohajeri, N., T-Raissi, A. & Adebeyi, O. Hydrolytic cleavage of ammonia-borane complex for hydrogen production. *J. Power Sources* **167**, 482–485 (2007).
- Minkina, V., Shabunya, S., Kalinin, V., Martynenko, V. & Smirnova, A. Long-term stability of sodium borohydrides for hydrogen generation. *Int. J. Hydrogen Energy* **33**, 5629–5635 (2008).
- Himmelberger, D. W., Yoon, C. W., Bluhm, M. E., Carroll, P. J. & Sneddon, L. G. Base-Promoted Ammonia Borane Hydrogen-Release. *J. Am. Chem. Soc.* **131**, 14101–14110 (2009).
- Ramachandran, P. V. *et al.* Preparation of ammonia borane in high yield and purity, methanolysis, and regeneration. *Inorg. Chem.* **46**, 7810–7817 (2007).
- Chen, W. *et al.* Structural and kinetic insights into Pt/CNT catalysts during hydrogen generation from ammonia borane. *Chem. Eng. Sci.* **192**, 1242–1251 (2018).
- Li, Y. *et al.* Polymeric Micelle Assembly for the Smart Synthesis of Mesoporous Platinum Nanospheres with Tunable Pore Sizes. *Angew. Chemie - Int. Ed.* **54**, 11073–11077 (2015).
- Şen, B. *et al.* Monodisperse Palladium Nanoparticles Assembled on Graphene Oxide with The High Catalytic Activity and Reusability in The Dehydrogenation of Dimethylamine-borane. *Int. J. Hydrogen Energy* **43**, 20176–20182, <https://doi.org/10.1016/j.ijhydene.2018.10.116> (2018).
- Tanyıldızı, S., Morkan, İ. & Özkar, S. Ceria supported copper(0) nanoparticles as efficient and cost-effective catalyst for the dehydrogenation of dimethylamine borane. *Mol. Catal.* **434**, 57–68 (2017).
- Jiang, Y. & Berke, H. Dehydrocoupling of dimethylamine-borane catalysed by rhenium complexes and its application in olefin transfer-hydrogenations. *Chem. Commun.* **0**, 3571–3573 (2007).
- Yurderi, M., Bulut, A., Zahmakiran, M., Gülcan, M. & Özkar, S. Ruthenium(0) nanoparticles stabilized by metal-organic framework (ZIF-8): Highly efficient catalyst for the dehydrogenation of dimethylamine-borane and transfer hydrogenation of unsaturated hydrocarbons using dimethylamine-borane as hydrogen source. *Appl. Catal. B Environ.* **160–161**, 534–541 (2014).
- Li, C. & Yamauchi, Y. Facile solution synthesis of Ag@Pt core-shell nanoparticles with dendritic Pt shells. *Phys. Chem. Chem. Phys.* **15**, 3490–3496 (2013).
- Li, C. *et al.* Pore-tuning to boost the electrocatalytic activity of polymeric micelle-templated mesoporous Pd nanoparticles. *Chem. Sci.* **10**, 4054–4061 (2019).
- Li, C. *et al.* Electrochemical Deposition: An Advanced Approach for Templated Synthesis of Nanoporous Metal Architectures. *Acc. Chem. Res.* **51**, 1764–1773 (2018).
- Çelik, B. *et al.* Nearly Monodisperse Carbon Nanotube Furnished Nanocatalysts as Highly Efficient and Reusable Catalyst for Dehydrocoupling of DMAB and C1 to C3 Alcohol Oxidation. *Int. J. Hydrogen Energy* **41**, 3093–3101 (2016).
- Sen, B. *et al.* Highly Efficient Polymer Supported Monodisperse Ruthenium-nickel Nanocomposites for Dehydrocoupling of Dimethylamine Borane. *J. Colloid Interface Sci.* **526**, 480–486 (2018).
- Sen, F., Karatas, Y., Gulcan, M. & Zahmakiran, M. Amine-stabilized platinum(0) nanoparticles: active and reusable nanocatalyst in the room temperature dehydrogenation of dimethylamine-borane. *RSC Adv.* **4**, 1526–1531 (2014).
- Li, C., Sato, T. & Yamauchi, Y. Electrochemical Synthesis of One-Dimensional Mesoporous Pt Nanorods Using the Assembly of Surfactant Micelles in Confined Space. *Angew. Chemie Int. Ed.* **52**, 8050–8053 (2013).
- Çelik, B. *et al.* Monodispersed palladium-cobalt alloy nanoparticles assembled on poly(N-vinyl-pyrrolidone) (PVP) as a highly effective catalyst for dimethylamine borane (DMAB) dehydrocoupling. *RSC Adv.* **6**, 24097–24102 (2016).
- Sen, B., Kuzu, S., Demir, E., Onal Okyay, T. & Sen, F. Hydrogen Liberation from The Dehydrocoupling of Dimethylamine-borane at Room Temperature by Using Novel and Highly Monodispersed RuPtNi Nanocatalysts Decorated with Graphene Oxide. *Int. J. Hydrogen Energy* **42**, 23299–23306 (2017).
- Sen, B., Kuzu, S., Demir, E., Akocak, S. & Sen, F. Highly monodisperse RuCo nanoparticles decorated on functionalized multiwalled carbon nanotube with the highest observed catalytic activity in the dehydrogenation of dimethylamine-borane. *Int. J. Hydrogen Energy* **42**, 23292–23298 (2017).
- Şen, B. *et al.* Polymer-graphene hybride decorated Pt nanoparticles as highly efficient and reusable catalyst for the dehydrogenation of dimethylamine-borane at room temperature. *Int. J. Hydrogen Energy* **42**, 23284–23291 (2017).
- Sen, B., Şavk, A. & Sen, F. Highly Efficient Monodisperse Pt Nanoparticles Confined in The Carbon Black Hybrid Material for Hydrogen Liberation. *J. Colloid Interface Sci.* **520**, 112–118 (2018).
- Friedrich, A., Drees, M. & Schneider, S. Ruthenium-catalyzed dimethylamineborane dehydrogenation: Stepwise metal-centered dehydrocyclization. *Chem. - A Eur. J.* **15**, 10339–10342 (2009).
- Sloan, M. E. *et al.* Homogeneous Catalytic Dehydrocoupling/Dehydrogenation of Amine-Borane Adducts by Early Transition Metal, Group 4 Metallocene Complexes. *J. Am. Chem. Soc.* **132**, 3831–3841 (2010).
- Sen, B., Kuzu, S., Demir, E., Yıldırım, E. & Sen, F. Highly efficient catalytic dehydrogenation of dimethyl ammonia borane via monodisperse palladium-nickel alloy nanoparticles assembled on PEDOT. *Int. J. Hydrogen Energy* **42**, 23307–23314 (2017).
- Si, Y. & Samulski, E. T. Exfoliated Graphene Separated by Platinum Nanoparticles. *Chem. Mater.* **20**, 6792–6797 (2008).
- Yin, M. *et al.* Tungsten carbide promoted Pd and Pd-Co electrocatalysts for formic acid electrooxidation. *J. Power Sources* **219**, 106–111 (2012).
- Sen, B., Kuzu, S., Demir, E., Akocak, S. & Sen, F. Monodisperse Palladium-nickel Alloy Nanoparticles Assembled on Graphene Oxide with The High Catalytic Activity and Reusability in The Dehydrogenation of Dimethylamine-borane. *Int. J. Hydrogen Energy* **42**, 23276–23283 (2017).
- Ataee-Esfahani, H., Nemoto, Y., Wang, L. & Yamauchi, Y. Rational synthesis of Pt spheres with hollow interior and nanosponge shell using silica particles as template. *Chem. Commun.* **47**, 3885 (2011).
- Kohn, W. & Sham, L. J. Self-Consistent Equations Including Exchange and Correlation Effects. *Phys. Rev.* **140**, A1133–A1138 (1965).
- Frisch, M. J. *et al.* Gaussian 09, Revision B.01. Gaussian 09, Revision B.01, Gaussian, Inc., Wallingford CT (2009).
- Becke, A. D. Density-functional exchange-energy approximation with correct asymptotic behavior. *Phys. Rev. A* **38**, 3098–3100 (1988).
- Lee, C., Yang, W. & Parr, R. G. Development of the Colle-Salvetti correlation-energy formula into a functional of the electron density. *Phys. Rev. B* **37**, 785–789 (1988).

38. Beedri, N. I. *et al.* Bilayered ZnO/Nb₂O₅ photoanode for dye sensitized solar cell. *Int. J. Mod. Phys. B* **32**, 1840046 (2018).
39. Kanchi, S. *et al.* Selectivity and sensitivity enhanced green energy waste based indirect- μ -solid phase extraction of carbaryl supported by DFT and molecular docking studies. *J. Mol. Liq.* **257**, 112–120 (2018).
40. Wang, H. *et al.* Shape- and Size-Controlled Synthesis in Hard Templates: Sophisticated Chemical Reduction for Mesoporous Monocrystalline Platinum Nanoparticles. *J. Am. Chem. Soc.* **133**, 14526–14529 (2011).
41. Li, C. *et al.* Emerging Pt-based electrocatalysts with highly open nanoarchitectures for boosting oxygen reduction reaction. *Nano Today* **21**, 91–105 (2018).
42. Fellah, M. F. A density functional theory study of hydrogen adsorption on Be-, Mg-, and Ca-exchanged LTL zeolite clusters. *J. Mol. Model.* **23**, 184 (2017).
43. Fellah, M. F. Adsorption of hydrogen sulfide as initial step of H₂S removal: A DFT study on metal exchanged ZSM-12 clusters. *Fuel Process. Technol.* **144**, 191–196 (2016).
44. Silvi, B. & Savin, A. Classification of chemical bonds based on topological analysis of electron localization functions. *Nature* **371**, 683–686 (1994).
45. Savin, A. *et al.* A New Look at Electron Localization. *Angew. Chemie Int. Ed. English* **30**, 409–412 (1991).
46. Fuentealba, P., Chamorro, E. & Santos, J. C. Chapter 5 Understanding and using the electron localization function. In *Theoretical and Computational Chemistry* 57–85, [https://doi.org/10.1016/S1380-7323\(07\)80006-9](https://doi.org/10.1016/S1380-7323(07)80006-9) (2007).
47. Sjöberg, P. & Politzer, P. Use of the electrostatic potential at the molecular surface to interpret and predict nucleophilic processes. *J. Phys. Chem.* **94**, 3959–3961 (1990).
48. Yu, G. *et al.* Theoretical and experimental evidence for rGO-4-PP Nc as a metal-free Fenton-like catalyst by tuning the electron distribution. *RSC Adv* **8**, 3312–3320 (2018).
49. Chandra, M. & Xu, Q. A high-performance hydrogen generation system: Transition metal-catalyzed dissociation and hydrolysis of ammonia–borane. *J. Power Sources* **156**, 190–194 (2006).
50. Şen, B. *et al.* Nanocarbon-supported catalysts for the efficient dehydrogenation of dimethylamine borane. In *Nanocarbon and its Composites*, <https://doi.org/10.1016/b978-0-08-102509-3.00020-1> (2019).

Author contributions

U.E. and F.S. organized all experiments and wrote the manuscript. O.A., B.S., A.S., S.D.M. and M.F.F. performed all experiments and characterizations. They have also drawn the figures.

Competing interests

The authors declare no competing interests.

Additional information

Supplementary information is available for this paper at <https://doi.org/10.1038/s41598-020-64221-y>.

Correspondence and requests for materials should be addressed to U.E. or F.S.

Reprints and permissions information is available at www.nature.com/reprints.

Publisher's note Springer Nature remains neutral with regard to jurisdictional claims in published maps and institutional affiliations.



Open Access This article is licensed under a Creative Commons Attribution 4.0 International License, which permits use, sharing, adaptation, distribution and reproduction in any medium or format, as long as you give appropriate credit to the original author(s) and the source, provide a link to the Creative Commons license, and indicate if changes were made. The images or other third party material in this article are included in the article's Creative Commons license, unless indicated otherwise in a credit line to the material. If material is not included in the article's Creative Commons license and your intended use is not permitted by statutory regulation or exceeds the permitted use, you will need to obtain permission directly from the copyright holder. To view a copy of this license, visit <http://creativecommons.org/licenses/by/4.0/>.

© The Author(s) 2020